Journal of Materials Chemistry C **2021**, *9 (19)*, 6268-6276

This paper must be cited as:
Kniec, K., Piotrowski, W., Ledwa, K., Suta, M., Carlos, L. D., Marciniak, L., Journal of Materials Chemistry C 2021, 9 (10), 6268-6276; doi: 10.1039/D1TC01272J.

From quencher to potent activator – Multimodal luminescence thermometry with Fe^{3+} in the oxides MAl_4O_7 (M = Ca, Sr, Ba)

by Karolina Kniec,[a] Wojciech Piotrowski,[a] Karolina Ledwa,[a] Markus Suta,[*,b,c] Luís Dias Carlos,[d] and Lukasz Marciniak,[*,a]

a. Institute of Low Temperature and Structure Research, Polish Academy of Sciences, Okólna 2, 50-422 Wroclaw, Poland.

b. Condensed Matter and Interfaces, Debye Institute for Nanomaterials Science, Department of Chemistry, Utrecht University, Princetonplein 1, 3584 CC Utrecht, Netherlands.

c. Inorganic Photoactive Materials, Department of Inorganic Chemistry, Heinrich Heine University Düsseldorf, Universitätsstraße 1, 40225 Düsseldorf, Germany.

d. Phantom-g, CICECO-Aveiro Institute of Materials, Department of Physics, University of Aveiro, Campus de Santiago, 3810-193 Aveiro, Portugal.

[*]E-mail: l.marciniak@intibs.pl, m.suta@uu.nl

Journal of Materials Chemistry C **2021**, *9 (19)*, 6268-6276

Abstract

Luminescence (nano)thermometry is an emerging and promising field for remote temperature sensing and thermal imaging of both the surface and interior of objects. While the field is dominated by trivalent lanthanide ions (Ln^{3+}) with their narrow $4f^n$-$4f^n$ transitions, the shielded nature of the 4f orbitals limits the tunability of the emission range and thermometric performance by the surrounding host. The transition metal ions besides the established $3d^3$ ions Cr^{3+} or Mn^{4+} have a so far underestimated role in that regard, although many of them do emit in the biologically relevant near-infrared range and their luminescence properties are far more sensitive to changes in the embedding host matrix than in the case of the Ln^{3+} ions. In this work, we demonstrate the potential of the abundant Fe^{3+} ion as a candidate for sensitive luminescence thermometry in the aluminate hosts MAl_4O_7 (M = Ca, Sr, Ba). Although this ion is usually considered an efficient luminescence quencher, it is shown that a targeted control of its luminescence properties makes this activator an interesting and only scarcely investigated alternative to the Ln^{3+} ions. We investigated the possibility for different modes of luminescence thermometry with Fe^{3+} (eventually co-doped with Tb^{3+} as internal thermally insensitive intensity reference), which include absolute intensity, ratiometric or lifetime thermometry. By selective changes in the Fe-O bond distances, it is possible to modulate the relative sensitivity towards values as high as around 2% K^{-1} at room temperature in $CaAl_4O_7$:Fe^{3+}, Tb^{3+} and connected relative temperature uncertainties of around 0.3%.

Introduction

The precise and fast detection of local temperature changes is crucial in controlling the proper functioning of diverse types of electronic and mechanical devices and systems. Such temperature measurements enable quick detection of local overheating points of mechanical parts, which is relevant from a diagnostic perspective. The specific and demanding operating conditions of such systems, such as high temperatures, extreme pH, the requirement of electrically noninterfering working mode preclude an application of conventional temperature sensors with macroscopic detectors in immediate contact with the heating spot. Based on that requirement, there has been a significant increase in research devoted to remote temperature readout in the last decade. A continuously emerging class of remote temperature sensors is luminescent thermometers. In contrast to other remote temperature sensing techniques such as thermography being only limited to thermal imaging of surfaces [1–3], luminescence thermometry overcomes this limitation and allows temperature mapping of the whole interior of a thermalized object. Luminescence thermometry (LT) exploits the thermally induced change of the spectroscopic properties of a phosphor to extract information about the local temperature[4–8]. Therefore, this approach does in principle enable real-time detection of the heating spots of the elements. The precision of the temperature determination in LT depends on the emission intensity of the phosphor and the relative sensitivity of the luminescent thermometer to temperature changes. Therefore, different types of host materials and luminescent dopant ions are currently examined to select the most promising candidates for remote temperature sensing applications. Among the inorganic host materials doped with luminescent ions, that are characterized by high thermal and chemical stability, a large group of luminescent thermometers exploits the difference in the temperature dependence of the optical response of lanthanide ions (Ln^{3+}) and transition metal ions (TM) as a measure for temperature itself. TM ions are usually efficient luminescent quenchers or, alternatively, prone to drastic thermal quenching in a certain temperature range that is governed by the surrounding host material. This usually undesired property does, however, make TM luminescence extremely suitable as a sensitive temperature probe if compared to an internal, thermally stable luminescence signal that does not interfere in the TM-based emission. A suited candidate for

https://doi.org/10.1039/D1TC01272J

such a thermally stable reference signal is the luminescence of Ln^{3+} ions, which then allows a ratiometric intensity readout. Ratiometric luminescence thermometry eliminates most of the systematic errors that affect absolute luminescence intensity such as sample alignment, incident excitation power etc. enhancing, thus, the precision of the temperature measurement[9]. Especially in the case of applications in the biological sector, both an efficient absorption and emission in the near-infrared (NIR) spectral range is desirable[10,11]. While the $4f^n$-$4f^n$ transitions of the Ln^{3+} ions are characteristic for the selected Ln^{3+} ion itself based on the shielded nature of the 4f orbitals by the more spatially extended 5s and 5p orbitals, the energy of the optical d^n-d^n transitions of TM ions can be much more controlled by the local chemical environment and site symmetry in an embedding host compound. However, a shift of the respective emission towards the NIR range is usually accompanied by very low quenching temperatures. This behavior results from the fact that the potentials of the excited d^n states typically lead to higher average equilibrium TM-ligand distances due to an excitation into more antibonding molecular orbitals. For emission in the NIR range, the crossing points between the ground and lowest excited potential are at very low energies in that case. Therefore, currently conducted works on TM-based luminescent thermometers aim at an enhancement of the emission intensity in the NIR range[12–14]. Among the most prominent candidates so far are the $3d^3$ ions Cr^{3+} and Mn^{4+} doped into oxidic host compounds[15–18]. However, also several other TM ions show intense NIR luminescence with large a large response to small temperature changes [19–28]. A promising and so far scarcely investigated candidate in that area is the abundant and chemically stable Fe^{3+} ion. In order to test its potential in the field of luminescence thermometry, we investigated in this work a series of low symmetric aluminates with the general formula of MAl_4O_7 (M= Ca, Sr, Ba). These compounds are characterized by a high thermal, mechanical and chemical stability [29], and have been mainly considered as host lattices for Ln^{3+} ions [30,31], which show durable persistent luminescence in conjunction with Eu^{2+} in there [32–39]. Moreover, they are considered as potential luminescent materials for lighting-oriented applications, such as fluorescent lamps, electroluminescence displays and light-emitting diodes (LEDs) [40,41], operating both in the UV and visible spectral range. However, they were definitely to a lesser extent considered as host materials for TM ions, since up to now, only Mn^{4+}-doped MAl_4O_7-type aluminates were studied [42], [43]. Based on the establishment as a host material for Ln^{3+}, we co-doped Tb^{3+} as an internal intensity reference standard, as it was already proposed by some of us[44]. It does only show thermal quenching effects at very high temperatures and the optical transitions of this ion do not interfere with the desirable NIR luminescence of Fe^{3+} that is sensitive to temperature changes.

Experimental

Synthesis

Synthesis of Fe^{3+}-doped nanocrystals.

The phosphors $SrAl_4O_7$ (SAO), $CaAl_4O_7$ (CAO) and $BaAl_4O_7$ (BAO) doped with 0.1 mol% Fe^{3+} ions (with respect to Al) have been successfully obtained using the modified Pechini method. Strontium nitrate hexahydrate ($Sr(NO_3)_2 \cdot 6H_2O$ Puratronic of 99.9965% purity from Alfa Aesar), calcium nitrate tetrahydrate ($Ca(NO_3)_2 \cdot 4H_2O$ of 99.999% purity from Alfa Aesar), barium nitrate hexahydrate ($Ba(NO_3)_2$ $6H_2O$ of 99.999% purity from Alfa Aesar), aluminum nitrate nonahydrate ($Al(NO_3)_3 \cdot 9H_2O$ of 99.999% purity from Alfa Aesar), iron(III) nitrate nonahydrate ($Fe(NO_3)_3 \cdot 9H_2O$ of 99.999% purity from Alfa Aesar) were used together with citric acid (CA, $C_6H_8O_7$ of 99.5+% purity from Alfa Aesar) and polyethylene glycol (PEG-200, from Alfa Aesar) as starting compounds. Appropriate amounts of the nitrates were dissolved in a small volume of distilled water (20 mL) and stirred with CA at 90 °C for 2 h using a magnetic stirrer on the heating stage. The starting materials for the synthesis of CAO and SAO were used in

https://doi.org/10.1039/D1TC01272J

stoichiometric quantities. The CA, acting as a complexing agent, was used in a double molar excess with respect to the total molar amount of all metal ions (Sr^{2+}/Ca^{2+}/Ba^{2+}, Al^{3+} and Fe^{3+}). Afterwards, an adequate volume of PEG-200 (1:1 molar ratio with respect to CA) was added dropwise to the aqueous solution of the metal complexes under vigorous stirring at 90 °C for 1 h. This step led to the polyesterification process between CA and PEG which forms a viscous medium that mechanically separates the forming nanoseeds of the aluminates. Then, the reaction mixture was transferred to a porcelain crucible and heated up to 250 °C to create the resin and thereafter to start the preliminary decomposition of organic compounds. The powdered colorless nanocrystals were obtained by annealing in air at 1000 °C for 12 h.
The Fe^{3+}, Tb^{3+} co-doped phosphors were synthesized using the same method as mentioned above. The terbium nitrate ($Tb(NO_3)_3 \cdot xH_2O$) was synthesized by dissolving terbium(III, IV) oxide (Tb_4O_7 of 99.999% purity from Stanford Materials Corporation) in concentrated nitric acid (65%) and recrystallization for additional purification. The appropriate starting materials including terbium(III) nitrate were mixed and treated as described above to produce the colorless powder containing the desired nanocrystals. The concentration of Fe^{3+} and Tb^{3+} was set to be 0.1 mol% with respect to the Al^{3+} and Ca^{2+}/Ba^{2+} ions, respectively.

Characterization

X-ray powder diffraction was carried out on a PANalytical X'Pert Pro diffractometer equipped with Anton Paar TCU 1000 N Temperature Control Unit using Ni-filtered Cu K_α radiation (V = 40 kV, I = 30 mA, λ = 1.54 nm).
The emission spectra were measured using the 266 nm excitation line from a laser diode (LD) and a Silver-Nova Super Range TEC Spectrometer from Stellarnet (1 nm spectral resolution) as a detector. The temperature of the sample was controlled using a THMS600 heating-cooling stage from Linkam Scientific (± 0.1 °C temperature stability and ± 0.1 °C set point resolution). Excitation spectra were measured using a FLS980 Fluorescence Spectrometer from Edinburgh Instruments with a 450 W Xenon lamp. Both the excitation and emission 300 mm focal length monochromators were in Czerny-Turner configuration. The excitation arm was supplied with a holographic grating of 1800 lines/mm, blazed at 250 nm, while the emission compartment was supplied with ruled grating, 1800 lines/mm blazed at 500nm. The spectral resolution was 0.1 nm. The R928P side window photomultiplier tube from Hamamatsu was sued as a detector. Luminescence decay profiles were recorded using an FLS1000 Fluorescence Spectrometer from Edinburgh Instruments with a μFlash lamp as an excitation source and R928P side window photomultiplier tube from Hamamatsu as a detector. Temperature-dependent luminescence decay traces were measured using the abovementioned heating-cooling stage from Linkam Scientific. Scanning electron microscopy (SEM) was performed on a Field Emission Scanning Electron Microscope (FEI Nova NanoSEM 230, FEI) equipped with an energy-dispersive spectrometer (EDAX Genesis XM4). Before the measurements, each sample had been dispersed in methanol, and then a droplet of a suspension was put on a carbon stub and dried under vacuum.

Results and Discussion

The XRD analysis was used to verify the crystallographic structure of synthesized materials doped with Fe^{3+} (Figure 1). The experimental patterns of synthesized materials agree with the reference reflections (Figure 1 a – c, see also Table 1). The evident phase purity of the investigated phosphors indicates that implemented synthesis method and its conditions can be successfully applied to obtain well-crystallized structures of presented aluminates. $CaAl_4O_7$ and $SrAl_4O_7$ crystallize in a monoclinic crystal system with the space group *C*2/*c* (no. 15). Their structures consist of layers formed by $[AlO_4]^{5-}$ tetrahedra and Sr^{2+}/Ca^{2+} ions, being embedded between these layers (Figure 1 d, e), where the Al^{3+} ions occupy sites with local C_1 symmetry

https://doi.org/10.1039/D1TC01272J

[45]. $BaAl_4O_7$ crystallizes in two different polymorphs with orthorhombic crystal systems each, namely *α*-$BaAl_4O_7$ and *β*-$BaAl_4O_7$, whose formation can be adjusted by changing the annealing temperature and time duration [46]. Within this work, the synthesized material corresponds to the *β*-$BaAl_4O_7$ polymorph crystallizing in a $Pm2_1n$ space group (no. 31) and local C_1 site symmetry of the Al^{3+} ions. The Sr^{2+} and Ca^{2+} ions occupy different crystallographic positions, namely their nearest neighbors are composed of five O^{2-} ions in the case of $SrAl_4O_7$, whereas of 7 O^{2-} ions in $CaAl_4O_7$. Both of these crystallographic surroundings are observed for Ba^{2+} ions in $BaAl_4O_7$ structure, creating large polyhedra that fill the channels formed by corner-sharing tetrahedra of $[AlO_4]^{4-}$ (Figure 1 i). Due to the ionic sizes and the same charge, we presume that the Fe^{3+} (r = 0.63 Å for a coordination number of 4 and high spin (HS) configuration) ions substitute the Al^{3+} ions (0.53 Å for coordination number of 4). Two crystallographic positions of Al^{3+} ions are present in the case of the $CaAl_4O_7$ and $SrAl_4O_7$ compounds (Al1, Al2), whereas four crystallographically distinguishable are present in the unit cell of $BaAl_4O_7$ (Al1, Al2, Al3, Al4).

The Fe^{3+} substitution leads to the slight shifts of the XRD reflections with respect to reference patterns (Figure. 1a). The XRD patterns (see Figure 1a) indicate the purity of all three aluminates. The transmission electron microscopy (TEM) images of synthesized materials confirm that obtained powders consist of well-crystallized particles (Figure S1 a-f). However, dependent on the host composition, the morphology of investigated phosphors differs. Thus, the Ba-based compounds are characterized by oblong structures, consisting of small and conglomerated crystallites (Figure S1 a, d). In contrast, the CAO and SAO powders consist of highly aggregated particles of irregular shapes (Figure S1b, c, e, f). This phenomenon is a consequence of elevated calcination temperature and long annealing time, which facilitates the diffusion processes during the growth of the nanoparticles. To examine thoroughly the morphology of synthesized materials of the larger area the as-prepared powders were analyzed with scanning electron microscopy (SEM). The histograms of particles size distribution indicate that the average particle size of CAO, SAO and BAO is around 200 nm, 400 nm and 450 nm, respectively, and clearly demonstrates that the powders are microcrystalline (Figure 1 j-l). No evident changes in the phase purity were observed for $CaAl_4O_7$ and $BaAl_4O_7$ structures after the simultaneous introduction of Fe^{3+}, Tb^{3+} - co-dopants (Figure S2). In this case, it is presumed that the large Tb^{3+} ions with an ionic radius of 1.18 Å preferentially occupy the seven-fold coordinated crystallographic sites of Ca^{2+} (r_{Ca} = 1.06 Å) and Ba^{2+} ions (r_{Ba} = 1.38 Å) [47].

Table 1. Structural parametric of investigated host materials

Parameter	**SAO**	**CAO**	**BAO**
ICSD code	716751	734487	424775
Crystal system	monoclinic	monoclinic	orthorhombic
Space group (no.)	*C*2/*c* (17)	*C*2/*c* (17)	$Pm2_1n$ (31)
a cell parameter [Å]	8.0850	8.7519	12.7735
Al^{3+} - O^{2-} distance [Å]	1.7556	1.7510	1.7476

https://doi.org/10.1039/D1TC01272J

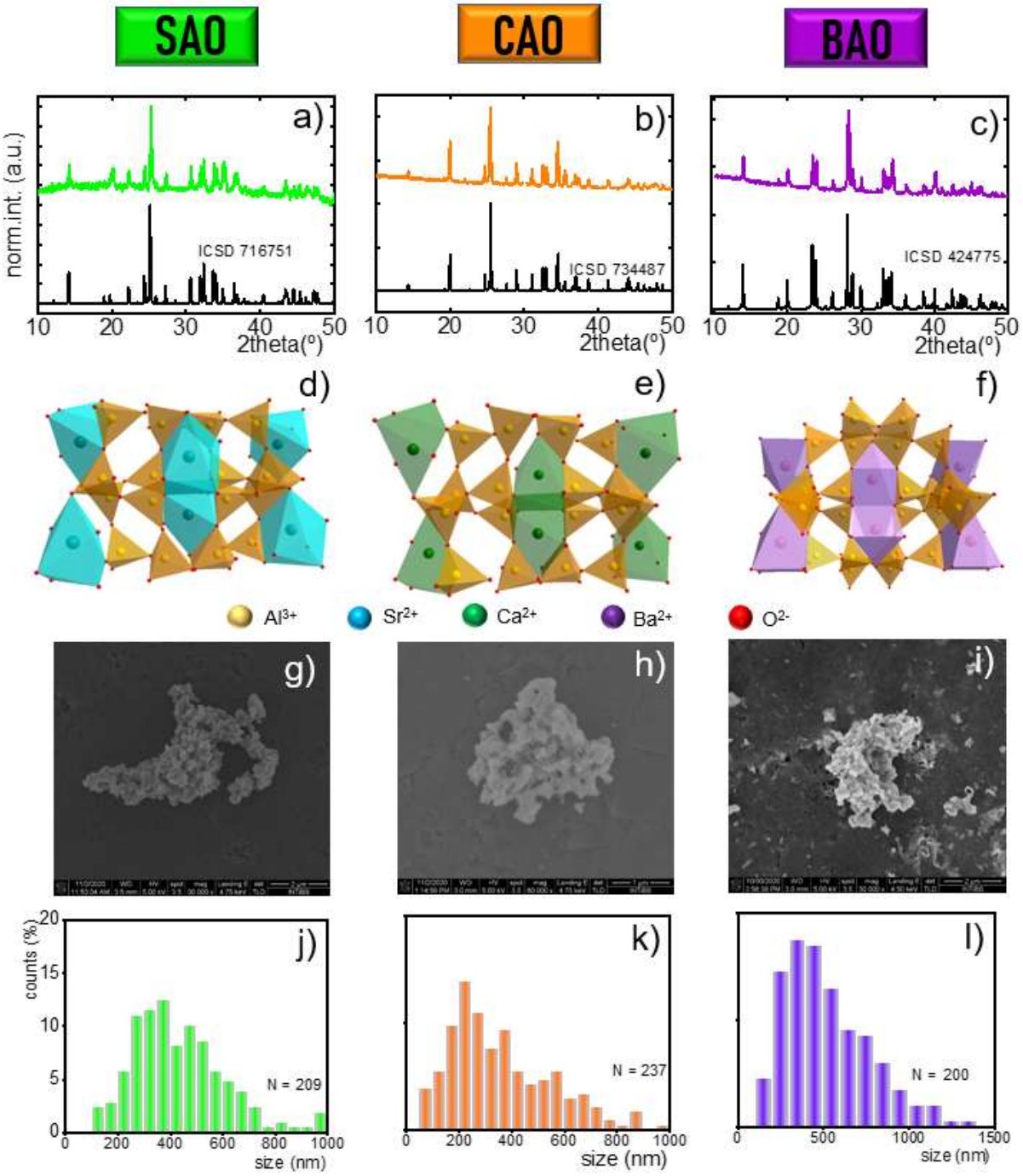

Figure 1. The XRD patterns of a) SAO:Fe^{3+}, b) CAO :Fe^{3+}, c) BAO:Fe^{3+} .Visualization of coordination spheres in the investigated host materials: d) SAO:Fe^{3+}, e) CAO:Fe^{3+}, f) BAO:Fe^{3+} . Representative SEM images of Fe^{3+}-activated aluminates: g) SAO:Fe^{3+}, h) CAO:Fe^{3+}, i) BAO:Fe^{3+} and histograms of particle size distributions of j) SAO:Fe^{3+}, k) CAO:Fe^{3+} and l) BAO:Fe^{3+} based on the SEM images.

To provide a better understanding of the optical properties of the Fe^{3+} ions in the investigated aluminates, the schematic configurational coordinate diagram of tetrahedrally coordinated Fe^{3+} ions is depicted in Figure 2a. In this case, the d^5 electronic configuration of Fe^{3+} ions is considered to be high-spin, which is energetically favorable since a tetrahedral crystal field splitting is small making a spin maximization thermodynamically more preferable. It was found that the crystal field strength significantly influences the spectral position of the Fe^{3+} emission band. In general, the Tanabe-Sugano (TS) diagram describes the dependence of the position of the energy levels of TM ions on the strength of the crystal field only for octahedral symmetry. However, due to the opposite splitting of d-orbitals in d^n tetrahedral and octahedral

https://doi.org/10.1039/D1TC01272J

configurations, the TS diagram for d^5 configuration can be used as a rough guideline to predict how the energy of the levels of tetrahedrally coordinates Fe^{3+} depends on the crystal field strength. In the conducted experiment, the UV excitation (λ_{exc} = 266 nm) leads to the appearance of a broad emission band localized in the NIR spectral range, attributed to the $^4T_1$ (^4G) → $^6A_1$ (^6S) $3d^5$-$3d^5$ electronic transition (Figure 2 b). The observed Fe^{3+} luminescence is efficiently excited upon excitation into the O^{2-} → Fe^{3+} charge-transfer transition. The excitation and emission spectra of SAO: Fe^{3+}, CAO: Fe^{3+} and BAO:Fe^{3+} measured at 123 K are depicted in Figure 2b and allow to elucidate structure-property relationships without significant contributions due to vibronic broadening of the respective bands. The emission energies strongly depend on the host composition. In the case of SAO:Fe^{3+}, the corresponding maximum is located at 13030 cm^{-1}, while gradually shifts to 12735 cm^{-1} in BAO:Fe^{3+} and 12653 cm^{-1} in CAO: Fe^{3+} (Figure 2c). In the case of octahedral coordination, the crystal field strength increases with decreasing average M-O distance *R* according to a R^{-5} dependence[48,49]. In the case of the d^5 electronic configuration the energy of the $^4T_1$ (^4G) state gradually decreases with an increase of the crystal field strength. This becomes evident upon the comparison of Fe^{3+} to the isoelectronic ion Mn^{2+}. The lower oxidation state of the Mn^{2+} ions in a HS configuration induces a generally weaker crystal field splitting. Thus, Mn^{2+} shows green luminescence when embedded in a tetrahedral coordination sphere[50], while the Fe^{3+} ions in the present study emit in the lower energetic NIR range. Although the Fe^{3+} ions are tetrahedrally coordinated in each of the MAl_4O_7 (M = Ca, Sr, Ba) compounds, a subtle variation of the emission energy of the Fe^{3+} ions is detectable, which is related to slightly different average Fe-O distances within the tetrahedra (Figure 2c inset). With a larger Fe-O distance as is the case in SAO, the emission is also located at higher energy given the weaker crystal field and the correspondingly higher energy of the lowest excited $^4T_1$(^4G) state. This makes optimization of the spectral position of the emission band based on the crystallographic parameters of the host compound possible [50]. In turn, in the excitation spectra recorded upon monitoring the $^4T_1$(^4G) → $^6A_1$ (^6S) emission, the broadband associated with $^6A_1$ (^6S) → $^4T_2$ (^4D) transition in the 320 nm – 350 nm spectral range dominates in CAO:Fe^{3+} and SAO: Fe^{3+} materials (Figure 2b). The same band was observed for the BAO:Fe^{3+} phosphors, however with a lower intensity. Another broad excitation band in the 250 - 310 nm spectral range is detected that is assigned to an O^{2-} → Fe^{3+} charge transfer transition. It has been already presented, that this band can lend intensity to the intraconfigurational d^5-d^5 transitions with similar energies [51]. However, the spectral position of its maximum depends on the host composition, namely it is shifted towards longer wavelengths in following order BAO:Fe^{3+} (277 nm - 36 105 cm^{-1} < SAO: Fe^{3+} (303 nm - 33 000 cm^{-1} < CAO: Fe^{3+} (308 nm - 32450 cm-1). The energy of the O^{2-} → Fe^{3+} charge transfer band is also related to the average bond Fe-O bond distance. In a simplistic molecular orbital (MO) picture, a shorter Fe-O bond would lead to a larger splitting between the more bonding MOs with dominant 2p contribution of the O^{2-} ions and the more antibonding MOs with dominant d(t_2) character of the Fe^{3+} (HS) ions, while the d(*e*)-type orbitals are majorly non-bonding. Consequently, a shorter Fe-O bond leads to a higher required ligand-to-metal charge transfer (LMCT) energy, as is also generally observed. In the case of BAO:Fe^{3+}, also other excitation bands related to d^5-d^5 electronic transitions are observable in the spectral ranges of 380 - 390 nm and 440 – 450 nm, respectively. Although a relatively low Fe^{3+} concentration was used the luminescence decay profiles slightly deviate from the exponential decay (Figure S3), which may be related to the presence of several crystallographically different Al^{3+} sites with a slightly different chemical environment. The luminescence decay profiles could be well fitted to a double exponential function. In that case, the average decay time can be calculated according to the following formula:

https://doi.org/10.1039/D1TC01272J

$$< \tau >= \frac{A_1\tau_1^2 + A_2\tau_2^2}{A_1\tau_1 + A_2\tau_2} \quad (1)$$

where τ_1, τ_2 are the separate luminescence decay time components, and A_1, A_2 are the respective weights of in the double exponential model profile. (see Eq. S1). The relatively long luminescence average decay times with the values of $\langle\tau\rangle$ = (3.91 ± 0.06) ms for SAO: Fe^{3+}, $\langle\tau\rangle$ = (3.80 ± 0.05) ms for CAO: Fe^{3+} and $\langle\tau\rangle$ = (4.16 ± 0.07) ms for BAO: Fe^{3+} (Figure 2d) can be related to the spin-forbidden character of the $^4T_1(^4G) \rightarrow {}^6A(^6S)$ transition and the only weak nature of spin-orbit coupling in a light TM ion like Fe^{3+}.

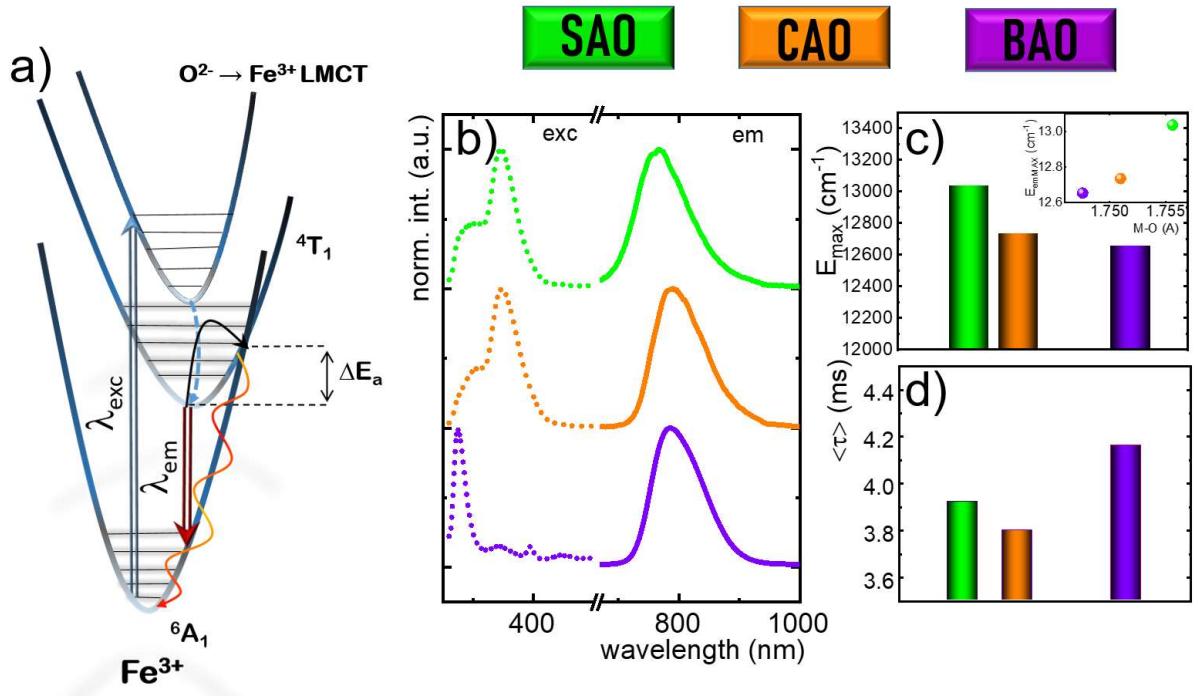

Figure 2. a) Schematic configurational coordinate diagram of the Fe^{3+} ions indicating the radiative and non-radiative quenching pathways. b) Excitation and emission spectra of Fe^{3+}-doped MAl_4O_7 (M = Ca, Sr, Ba) recorded at 123 K. c) Energy of the $^4T_1$ (^4G) → $^6A_1$ emission maxima at 123 K. The inset depicts the energy of the maxima of the emission band as a function of the M-O distance. d) Average luminescence lifetime of the Fe^{3+}-doped aluminates at 123 K.

In order to evaluate the capability of the MAl_4O_7 :Fe^{3+} phosphors to luminescence thermometry, their emission spectra were measured in a temperature range between 123 and 573 K (Figures 3a – c). The Fe^{3+}-based luminescence intensity of all investigated compounds decreases along with increasing temperature, as a consequence of an increasing probability for non-radiative relaxation to the $^6A(^6S)$ ground state. In the case of BAO:Fe^{3+}, an evident blue shift of the emission maxima at elevated temperatures is observed. The Jacobian transformation of the emission spectra to an energy scale makes the presence of inhomogeneous broadening of the emission band in especially CAO:Fe^{3+} and BAO:Fe^{3+} evident (Figure 4). This additionally suggests that more than one emitting center is present in those phosphors, which can be discussed in terms of the substitution of the Fe^{3+} ions in different crystallographic positions of Al^{3+} ion in those host materials. In the case of the SAO only two Al^{3+} sites of relatively similar M-O distances were reported, while four Al^{3+} sites have been reported for BAO[37,42,46]. In the case of CAO two Al^{3+} sites are present, however, the difference in the average M-O distance calculated for this host material is larger than the one observed in SAO. The temperature dependence of the integrated emission intensity of MAl_4O_7:Fe^{3+} (M = Ca, Sr, Ba) phosphors

https://doi.org/10.1039/D1TC01272J

indicates that in the low-temperature range (below 220 K), most of the luminescence was efficiently thermally quenched in BAO:Fe^{3+}, while the Fe^{3+}-based luminescence was most stable in SAO:Fe^{3+}. Above 220 K, the thermal quenching rate of BAO:Fe^{3+} slows down and the integrated emission intensity in CAO:Fe^{3+} and SAO:Fe^{3+} continuously decreases with increasing temperature. It is noteworthy that the rate of the thermally activated nonradiative depopulation of the $^4T_1$ excited state is dependent on a subtle interplay between the crystal field strength and the strength of the Fe-O bonds . While a weak crystal field makes the $^4T_1$ – ^6A gap larger and thus, effectively increases the thermal activation barrier for a thermal crossover process, a gradually weaker chemical bond with flatter potential and higher Fe-O equilibrium distance in the $^4T_1(^4G)$ state counteracts and decreases the crossover barrier to the $^6A_1(^6S)$ state. It will be an interplay of both effects. Therefore, in the case of the SAO:Fe^{3+} luminescence still remains even at 570 K, while it is totally quenched at 410 K in the case of CAO:Fe^{3+}. In order to quantify the performance of thermally quenched emission intensity Fe^{3+}-doped aluminates as a measure for luminescence thermometry, the relative thermal sensitivity (S_R, in units of % · K^{-1}) was calculated as follows[5]:

$$S_R = \frac{1}{\Omega}\frac{\Delta\Omega}{\Delta T} \qquad (2)$$

where Ω represents the thermometric parameter and $\Delta\Omega$ corresponds to the change of Ω in the temperature interval ΔT. As shown in Figure 3e, the highest S_R (S_m) for the single intensity-based luminescent thermometer was found for BAO:Fe^{3+} at 163 K with a value of S_m = 3.22% K^{-1}. However, above this temperature, the relative sensitivity of the quenched Fe^{3+}-based luminescence in BAO drastically decreases reaching 0.36% K^{-1} at 265 K before it slightly increases at elevated temperatures again. On the other hand the maximum relative sensitivity for CAO:Fe^{3+} was S_m=2.89% K^{-1} at 297 K. However, in this case, the temperature range in which high sensitivity was observed was significantly wider (S_R > 1% K^{-1} in the 151 – 380 K range). High thermal stability of the Fe^{3+} emission intensity is realized in SAO:Fe^{3+}, which is also accompanied to a low S_R of maximum S_m = 0.94 % K^{-1} at 590 K. As important as the relative sensitivity is the intensity of the regarded emission band as the overall temperature precision depends on both factors. Thus, above 400 K the CAO:Fe^{3+} cannot be considered for applications due to the completely quenched luminescence (Figure 3). Although the S_R values for the MAl_4O_7:Fe^{3+} (M = Ca, Sr, Ba) intensity-based luminescent thermometer are quite appealing, the overall low reliability of absolute intensity measurements for remote temperature sensing prevents a final application. For a potential improvement of these Fe^{3+}-activated phosphors, the excited state kinetics of Fe^{3+} was analyzed in order to develop a lifetime-based thermometers. The luminescence decay profiles were measured in a 123 – 573 K range (Figure S5) and the average decay times as a function of the temperature (Figure 3f) were calculated using eq. (1)). In the case of the CAO:Fe^{3+} and SAO:Fe^{3+} , the luminescence decay time related to emission from the $^4T_1$ (^4G) decreases to 1.15 ms and 0.63 ms at 570 K, respectively. However in the case of the BAO:Fe^{3+}, a strong reduction of the luminescence decay time from 6.28 ms at 123 K to around 1 ms at 300K. Therefore the highest values of the S_R for the lifetime-based thermometry were found in BAO:Fe^{3+}. The maximal values of S_R reached 1.57 % K^{-1} at 258 K quickly decreasing to 0.82 %K^{-1} at 560 K for SAO:Fe^{3+} and 0.61% K^{-1} at 520 K for CAO:Fe^{3+}. This result indicates a high thermometric performance of BAO:Fe^{3+} for remote temperature sensing in a decay time-based approach. The difference in the luminescence thermal quenching rate of the Fe^{3+} ions localized in two crystallographically different Al^{3+} sites suggests that their emission intensity ratio can be used as a thermometric parameter in a ratiometric approach. Therefore, the temperature dependence of the

https://doi.org/10.1039/D1TC01272J

luminescence intensity ratio (LIR) defined below was examined as a function of temperature (Figure S9 a):

$$LIR = \frac{Fe^{3+}(^4T_1 \rightarrow {}^6A_1)}{Fe^{3+}(^4T_1 \rightarrow {}^6A_1)} = \frac{\int_{775nm}^{765nm} I_{em}(\lambda)\mathrm{d}\lambda}{\int_{800nm}^{810nm} I_{em}(\lambda)\mathrm{d}\lambda} \qquad (3)$$

That LIR increases significantly up to 223 K, above which its growth rate becomes slower. This thermal LIR dependence between 123 and 223 K is a consequence of the strong thermally induced luminescence response of the Fe^{3+} ions in the two different crystallographic Al1 and Al3 sites, whereas, at higher temperatures than 223 K, the emission intensity at 770 nm decreases less rapidly than the intensity at 806 nm. The relative thermal sensitivity increases to a maximum value of 3.52% K^{-1} up to 180 K (Figure S9 b) and still remains > 1% K^{-1} even up to 223 K.

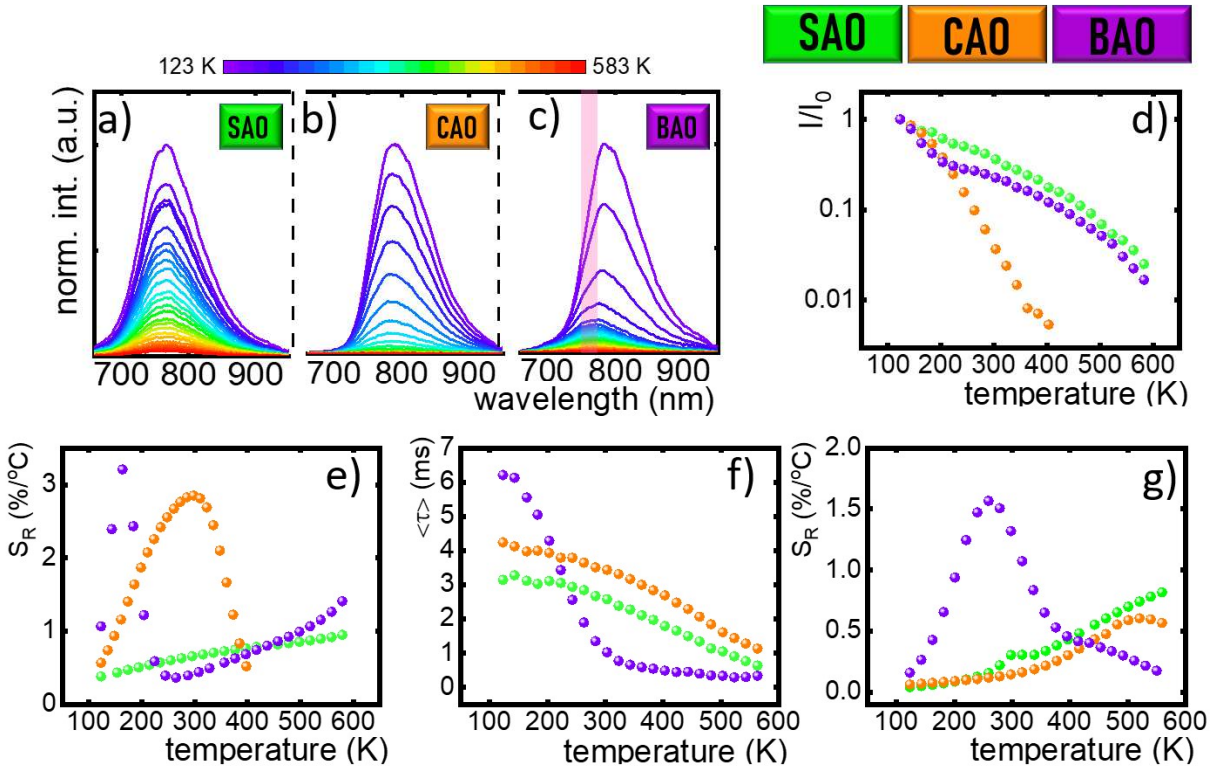

Figure 3. Temperature-dependent luminescence spectra of a) SAO:Fe^{3+}, b) CAO :Fe^{3+} and c) BAO:Fe^{3+} upon excitation at 266 nm. d) Normalized integrated intensity of the Fe^{3+}-based luminescence as a function of temperature. e) Temperature dependence of S_R for the intensity-based thermometry concept. f) Temperature-dependent average luminescence decay times $\langle\tau\rangle$ for SAO:Fe^{3+}, CAO :Fe^{3+}, BAO:Fe^{3+}. g) Temperature dependence of S_R for the lifetime-based concept.

A ratiometric approach with an internal and thermally stable luminescence reference was chosen as a way to improve the temperature sensing reliability of Fe^{3+}-based luminescence thermometers. Ln^{3+} ions prove useful for this approach since at low doping concentrations, multi-phonon relaxation of the excited $4f^n$ states is the dominant process of their luminescence thermal quenching. Thus, a very large energy gap between excited and the next lower energy level is beneficial for this concept. A particularly suited candidate with yet visible luminescence is Tb^{3+} for which the relatively high thermal stability is expected. Therefore, Tb^{3+} ions were used in this study as co-dopants. An additional advantage of using Tb^{3+} ions as an internal luminescence reference in the Fe^{3+} doped luminescent thermometers is the fact that the most

intense Tb^{3+} emission at 540 nm ($^5D_4 \rightarrow {}^7F_5$) does not interfere with the Fe^{3+}-based emission in the NIR spectral range. This facilitates a ratiometric temperature readout. Obviously, the thermal stability of the Tb^{3+} may be affected by the $Tb^{3+} \rightarrow Fe^{3+}$ or $Fe^{3+} \rightarrow Tb^{3+}$ energy transfer, which enhances the thermometric performance of the Fe^{3+}, Tb^{3+} ratiometric luminescent thermometer, respectively.

In order to evaluate this approach, the two luminescent thermometers with the highest S_R have been co-doped with Tb^{3+} ions. The spectroscopic properties of the Fe^{3+}, Tb^{3+}-co-doped CAO and BAO were investigated between 123 K and 573 K upon UV excitation (266 nm) (Figure 4 a, b), which allows a simultaneous excitation of the emission originating from both Tb^{3+} and Fe^{3+}. In contrast to the broad emission band located in the NIR range due to Fe^{3+}, the emission spectrum of the co-doped Tb^{3+} ions is characterized by narrow bands with maxima at 490, 543, 589 and 625 nm. These are attributed to the electronic transition from the excited $^5D_4$ level to the $^7F_6$, $^7F_5$, $^7F_4$ and $^7F_3$ ground levels of Tb^{3+}, respectively (Figure 4 b, c).

While any temperature change strongly affects the Fe^{3+}-based emission intensity, the intensity of the Tb^{3+}-related luminescence is largely affected by the host composition. It is only slightly affected by the temperature in the whole analyzed range in the case of BAO: Fe^{3+}, Tb^{3+}, whereas it undergoes a stronger luminescence thermal quenching in the case of CAO: Fe^{3+}, Tb^{3+}. This phenomenon can be explained by the type of excitation of the Tb^{3+} ions. In the case of the CAO:Fe^{3+}, Tb^{3+}, the low absorption cross-section of the Tb^{3+} ions at 266 nm makes a $Fe^{3+} \rightarrow Tb^{3+}$ energy transfer the most effective population pathway of the radiatively emitting $^5D_4$ level of Tb^{3+}. Thus, the thermally induced depopulation of the excited states of the Fe^{3+} also affects the intensity of the Tb^{3+} luminescence. To verify the suitability of Fe^{3+}, Tb^{3+}-co-doped CAO and BAO for improved ratiometric thermometry, a LIR_2 parameter defined as the intensity ratio between Fe^{3+}- and Tb^{3+}-related emissions is considered (Figure 4d). It is observed that the evolution of the as-defined LIR_2 with increasing temperatures (Figure 4d) and that of the Fe^{3+} emission intensity alone (Figure 3d) are generally very similar. The LIR_2 decreases with a smaller rate at elevated temperatures, however, which results from a slight decrease of the Tb^{3+}-based emission intensity with increasing temperature. Hence, the maximum values of the connected relative thermal sensitivities are lower compared to the intensity-based thermometry approach with solely Fe^{3+}. The highest relative thermal sensitivities of the Fe^{3+}, Tb^{3+} co-doped thermometer is S_m = 1.56 % K^{-1} for BAO:Fe^{3+},Tb^{3+} at 140 K. It should be noted that in the 123 K – 400 K range, S_R was always higher than 1.50% K^{-1} and reached a maximum S_m = 2.08% K^{-1} at 373 K, which is clearly useful for applications. Additionally, a very low relative temperature uncertainty[5] (Suporting Information) in the CAO:Fe^{3+},Tb^{3+} (< ±0.5% between 100 K and 500 K) and BAO:Fe^{3+},Tb^{3+} (< ±2.0% between 100 K and 500 K) luminescent thermometers confirms their high thermometric performance (Figure S6).

The thermometric performance of MAl_4O_7:Fe^{3+} doped phosphors in different temperature readout modes is summarized in Table 2. Although very promising results have been obtained in the Fe^{3+} intensity-based approach, its liability towards other experimental impacts such as incident excitation power or doping concentration discredits this readout mode from practical implementation. Nevertheless, the high S_R values obtained in the case of the CAO and BAO for other thermometric approaches make them promising candidates for luminescence thermometry.

https://doi.org/10.1039/D1TC01272J

Table 2. Comparison of the maximum S_R values of Fe^{3+}-doped MAl_4O_7 (M = Ca, Sr, Ba) phosphors for differentthermometric measures.

Approach	SAO	CAO	BAO
Fe^{3+} intensity	0.94% K^{-1} at 590 K	2.89% K^{-1} at 297 K	3.22% K^{-1} at 163 K
LIR Fe^{3+} to Fe^{3+}	-	-	3.52% K^{-1} at 180 K
Luminescence decay	0.82% K^{-1} at 560 K	0.61% K^{-1} at 520 K	1.57 % K^{-1} at 258 K
LIR (Fe^{3+} to Tb^{3+})	-	2.08% K^{-1} at 373K	1.56 % K^{-1} at 140K

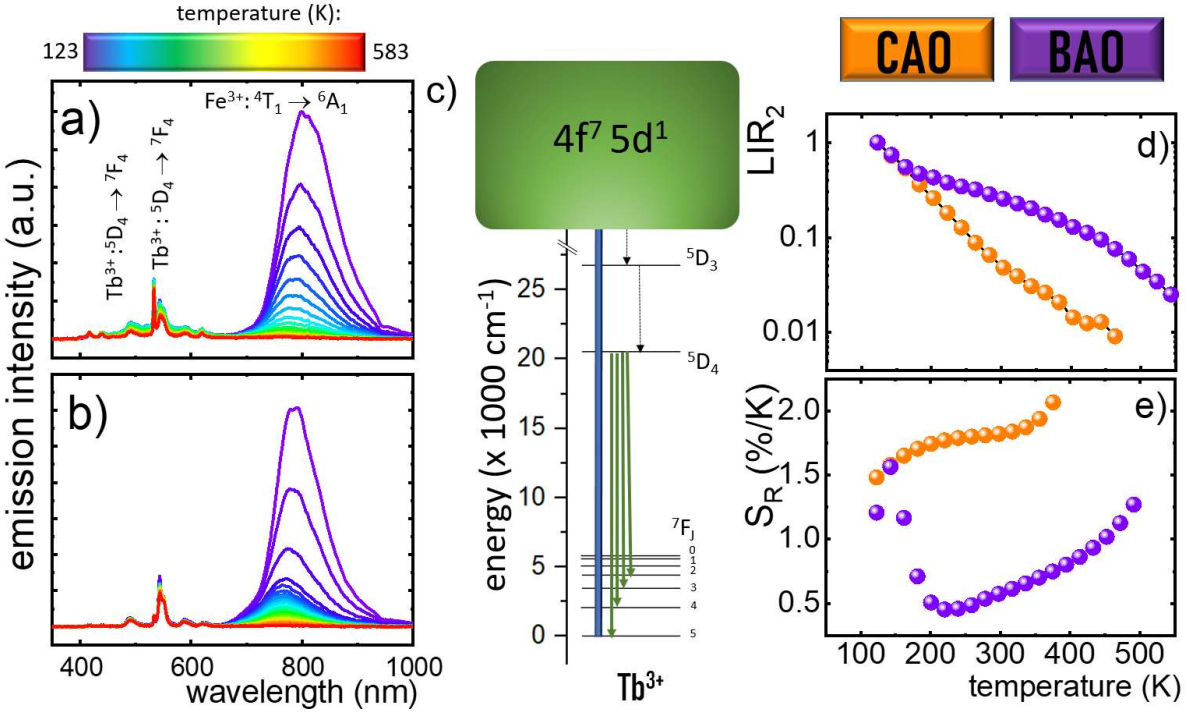

Figure 4. The temperature-dependent emission spectra of a) of CAO :Fe^{3+},Tb^{3+}–and b) BAO:Fe^{3+},Tb^{3+} upon excitation with 266 nm. c) Simplified schematic energy diagrams of Tb^{3+} ions. d) LIR as a function of temperature and e) corresponding S_R of CAO:Fe^{3+},Tb^{3+} and BAO:Fe^{3+},Tb^{3+}.

Conclusions

The potential of Fe^{3+} ions as remote luminescent thermometers was investigated in detail regarding the aluminates MAl_4O_7 (M = Ca, Sr, Ba) as representative host compounds. Microcrystalline powders of the Fe^{3+}-activated aluminates were synthesized using the modified Pechini method. Their spectroscopic properties were investigated in a wide range, 123 K to 573 K. It was found that the strong tendency of the observed broad NIR emission band associated with the $^4T_1(^4G) \rightarrow {}^6A_1(^6S)$ electronic transition of the incorporated Fe^{3+} ions to thermal quenching can be exploited as a highly sensitive luminescence thermometry concept. With increasing Fe-O distance, the energy of the Fe^{3+}-based emission also increases due to the gradually weaker crystal field strength that enhances the energy difference between the ground $^6A_1(^6S)$ and lowest excited $^4T_1(^4G)$ state, which allows tailoring the emission energy of Fe^{3+} towards the biologically relevant NIR spectral range. As a consequence of these structural impacts, the Fe^{3+}-related luminescence intensity in the case of SAO:Fe^{3+} was rather stable towards luminescence quenching given the high $^6A_1$-$^4T_1$ energy gap that makes non-radiative

https://doi.org/10.1039/D1TC01272J

thermal crossover only effective at very high temperatures (> 500 K). In contrast, the respective emission was effectively quenched in CAO:Fe^{3+} above 223 K and even below that temperature in the case of BAO:Fe^{3+}. The difference in their thermal quenching rates enables the development of a simple single band-based luminescence thermometry concept with a promising relative sensitivity of S_R = 2.89 % K^{-1} in CAO:Fe^{3+} at physiological temperatures.The strong temperature dependence of the average lifetime of the $^4T_1$ (^4G) state of Fe^{3+} in the ms range offers an alternative temperature sensing concept with maximum relative sensitivities of 1.57 % K^{-1} at 258 K in BAO.Fe^{3+}, 0.82% K^{-1} at 560 K in SAO:Fe^{3+} and 0.61% K^{-1} at 520 K in CAO:Fe^{3+}, respectively. Finally, upon the incorporation of Tb^{3+} ions as a thermally robust internal luminescence intensity standard with non-interfering green luminescence, it is possible to exploit the Fe^{3+}-related luminescence in a ratiometric thermometry approach less liable to systematic experimental errors. With that strategy, maximal S_R values of 2.08% K^{-1} at 373K for CAO:Fe^{3+}, Tb^{3+} and 1.56 % K^{-1} at 140 K for BAO:Fe^{3+}, Tb^{3+} were found. In the case of CAO:Fe^{3+}, Tb^{3+}, the combined large relative sensitivity with yet appreciable intensity of the Fe^{3+}-based emission leads to a relative temperature uncertainty below ±0.5% in the range between 100 K and 500 K. Thus, systematic structure-property investigations in the presented Fe^{3+}-activated aluminates do not only show a so far unexplored potential of the abundant Fe^{3+} ion as an effective luminescent thermometer, but even allow a targeted optimization towards desirable applications in e.g. the biomedical or microelectronic sector

Acknowledgements

The „High sensitive thermal imaging for biomedical and microelectronic application" project is carried out within the First Team program of the Foundation for Polish Science co-financed by the European Union under the European Regional Development Fund. M. S. and L. D. C. acknowledge funding from the European Union Horizon 2020 FET-Open program NanoTBTech (grant agreement no.: 801305).

References

[1] Y. Xiao, C. Wan, A. Shahsafi, J. Salman, Z. Yu, R. Wambold, H. Mei, B. E. R. Perez, W. Derdeyn, C. Yao, M. A. Kats, *Laser & Photonics Reviews* **2020**, *14*, 1900443.

[2] S. Yakunin, B. M. Benin, Y. Shynkarenko, O. Nazarenko, M. I. Bodnarchuk, D. N. Dirin, C. Hofer, S. Cattaneo, M. V Kovalenko, *Nature Materials* **2019**, *18*, 846.

[3] V. Morad, S. Yakunin, B. M. Benin, Y. Shynkarenko, M. J. Grotevent, I. Shorubalko, S. C. Boehme, M. V. Kovalenko, *Advanced Materials* **2021**, *33*, 2007355.

[4] M. Dramićanin, in *Woodhead Publishing Series in Electronic and Optical Materials* (Ed.: M.B.T.-L.T. Dramićanin), Woodhead Publishing, **2018**, pp. 251–263.

[5] C. D. S. Brites, S. Balabhadra, L. D. Carlos, **2018**, *1801239*, 1.

[6] D. Jaque, F. Vetrone, *Nanoscale* **2012**, *4*, 4301.

[7] A. Bednarkiewicz, L. Marciniak, L. D. Carlos, D. Jaque, *Nanoscale* **2020**, *12*, 14405.

[8] M. Suta, A. Meijerink, *Advanced Theory and Simulations* **2020**, *3*, 2000176.

[9] C. D. S. Brites, P. P. Lima, N. J. O. Silva, A. Millán, V. S. Amaral, F. Palacio, L. D. Carlos, *Advanced Materials* **2010**, *22*, 4499.

[10] A. M. Smith, M. C. Mancini, S. Nie, *Nature Nanotechnology* **2009**, *4*, 710.

[11] E. Hemmer, A. Benayas, F. Légaré, F. Vetrone, *Nanoscale Horizons* **2016**, *1*, 168.

[12] M. Back, J. Ueda, M. G. Brik, T. Lesniewski, M. Grinberg, S. Tanabe, *ACS Applied Materials and Interfaces* **2018**, *10*, 41512.

[13] K. Elzbieciak, L. Marciniak, *Frontiers in Chemistry* **2018**, *6*, 424.

[14] L. Marciniak, A. Bednarkiewicz, D. Kowalska, W. Strek, *Journal of Materials Chemistry C* **2016**, *4*, 5559.

[15] M. Back, J. Ueda, J. Xu, K. Asami, M. G. Brik, S. Tanabe, *Advanced Optical Materials* **2020**, *8*, 1.

[16] V. B. Mykhaylyk, H. Kraus, Y. Zhydachevskyy, V. Tsiumra, A. Luchechko, A. Wagner, A. Suchocki, *Sensors (Switzerland)* **2020**, *20*, 1.

[17] M. D. Dramićanin, B. Milićević, V. Đorđević, Z. Ristić, J. Zhou, D. Milivojević, J. Papan, M. G. Brik, C.-G. Ma, A. M. Srivastava, M. Wu, *ChemistrySelect* **2019**, *4*, 7067.

[18] W. Piotrowski, K. Trejgis, K. Maciejewska, K. Ledwa, B. Fond, L. Marciniak, *ACS Applied Materials & Interfaces* **2020**, *12*, 44039.

[19] K. Kniec, L. Marciniak, *Physical Chemistry Chemical Physics* **2018**, *20*, 21598.
[20] A. Kobylinska, K. Kniec, K. Maciejewska, L. Marciniak, *New Journal of Chemistry* **2019**, *43*, 6080.
[21] C. Matuszewska, K. Elzbieciak-Piecka, L. Marciniak, *Journal of Physical Chemistry C* **2019**, *123*, 18646.
[22] J. Drabik, Ł. Marciniak, B. B. Cichy, L. Marciniak, *Journal of Physical Chemistry C* **2018**, *122*, 14928.
[23] F. Li, J. Cai, F. F. Chi, Y. Chen, C. Duan, M. Yin, *Optical Materials* **2017**, *66*, 447.
[24] L. Marciniak, A. Bednarkiewicz, *Sensors and Actuators B: Chemical* **2017**, *243*, 388.
[25] E. Glais, C. Chanéac, B. Viana, in *Optics InfoBase Conference Papers*, **2019**, p. 1.
[26] K. Kniec, K. Ledwa, K. Maciejewska, L. Marciniak, *Materials Chemistry Frontiers* **2020**, *4*, 1697.
[27] K. Maciejewska, L. Marciniak, *Chemical Engineering Journal* **2020**, *402*, 126197.
[28] K. Maciejewska, B. Poźniak, M. Tikhomirov, A. Kobylińska, L. Marciniak, *Nanomaterials* **2020**, *10*, 421.
[29] M. Puchalska, E. Zych, A. Watras, *Journal of Luminescence* **2017**, *183*, 185.
[30] D. Dutczak, T. Jüstel, C. Ronda, A. Meijerink, *Physical Chemistry Chemical Physics* **2015**, *17*, 15236.
[31] M. Puchalska, A. Watras, *Journal of Alloys and Compounds* **2016**, *688*, 253.
[32] A. N. Yerpude, S. J. Dhoble, *Optik* **2016**, *127*, 4217.
[33] M. Misevicius, V. Balevicius, *Materials Chemistry and Physics* **2020**, *249*, 122998.
[34] B. Cheng, Z. Zhang, Z. Han, Y. Xiao, S. Lei, *CrystEngComm* **2011**, *13*, 3545.
[35] T. Katsumata, K. Sasajima, T. Nabae, S. Komuro, T. Morikawa, *Journal of the American Ceramic Society* **2005**, *81*, 413.
[36] N. K. Giri, S. K. Singh, D. K. Rai, S. B. Rai, *Applied Physics B* **2010**, *99*, 271.
[37] V. Singh, S. Tamboli, S. J. Dhoble, H. Jeong, *Optik* **2020**, *213*, 164375.
[38] V. Singh, S. Kaur, M. Jayasimhadri, *Solid State Sciences* **2020**, *101*, 106049.
[39] D. Van der Heggen, D. Vandenberghe, N. K. Moayed, J. De Grave, P. F. Smet, J. J. Joos, *Journal of Luminescence* **2020**, *226*, 117496.
[40] V. Singh, G. Lakshminarayana, A. Wagh, *Optik* **2020**, *204*, 163908.
[41] A. S. Kumar, R. A. Kumar, R. R. Bhattacharjee, *Journal of Luminescence* **2017**, *182*, 130.
[42] R. Cao, Q. Xiong, W. Luo, D. Wu, X. Fen, X. Yu, *Ceramics International* **2015**, *41*, 7191.
[43] S. X. Liu, F. B. Xiong, H. F. Lin, X. G. Meng, S. Y. Lian, W. Z. Zhu, *Optik* **2018**, *170*, 178.
[44] K. Kniec, W. Piotrowski, K. Ledwa, L. D. Carlos, L. Marciniak, *Journal of Materials Chemistry C* **2021**, *9*, 517.
[45] M. Puchalska, E. Zych, M. Sobczyk, A. Watras, P. Deren, *Materials Chemistry and Physics* **2014**, *147*, 304.
[46] M. Allix, S. Alahrache, F. Fayon, M. Suchomel, F. Porcher, T. Cardinal, G. Matzen, *Advanced Materials* **2012**, *24*, 5570.
[47] R. D. Shannon, *Acta Crystallographica Section A* **1976**, *32*, 751.
[48] G. Burns, J. D. Axe, *The Journal of Chemical Physics* **1966**, *45*, 4362.
[49] M. Bermejo, L. Pueyo, *The Journal of Chemical Physics* **1983**, *78*, 854.
[50] V. Morad, I. Cherniukh, L. Pöttschacher, Y. Shynkarenko, S. Yakunin, M. V Kovalenko, *Chemistry of Materials* **2019**, *31*, 10161.
[51] V. Lupei, M. J. Elejalde, A. Brenier, G. Boulon, *Journal De Physique* **1994**, *4*, 329.

https://doi.org/10.1039/D1TC01272J